NANO LETTERS
Letter
Cite This: Nano Lett. 2018, 18, 6882−6891
pubs.acs.org/NanoLett

Intravalley Spin−Flip Relaxation Dynamics in Single-Layer WS_2

Zilong Wang,[†,#] Alejandro Molina-Sánchez,[‡,#] Patrick Altmann,[†,#] Davide Sangalli,[¶] Domenico De Fazio,[§] Giancarlo Soavi,[§] Ugo Sassi,[§] Federico Bottegoni,[†] Franco Ciccacci,[†] Marco Finazzi,[†] Ludger Wirtz,[∥] Andrea C. Ferrari,[*,§] Andrea Marini,[¶] Giulio Cerullo,[†,⊥] and Stefano Dal Conte[†]

[†]Department of Physics, Politecnico di Milano, Piazza Leonardo da Vinci 32, I-20133 Milano, Italy
[‡]Institute of Materials Science (ICMUV), University of Valencia, Catedrático Beltrán 2, E-46980 Valencia, Spain
[¶]CNR-ISM, Division of Ultrafast Process in Materials (FLASHit), Area della Ricerca di Roma 1, Monterotondo Scalo, Italy
[§]Cambridge Graphene Centre, University of Cambridge, 9 JJ Thomson Avenue, Cambridge CB3 0FA, U.K.
[∥]Université du Luxembourg, 162 A, avenue de la Faencerie, Luxembourg City L-1511, Luxembourg
[⊥]IFN-CNR, Piazza Leonardo da Vinci 32, I-20133 Milano, Italy

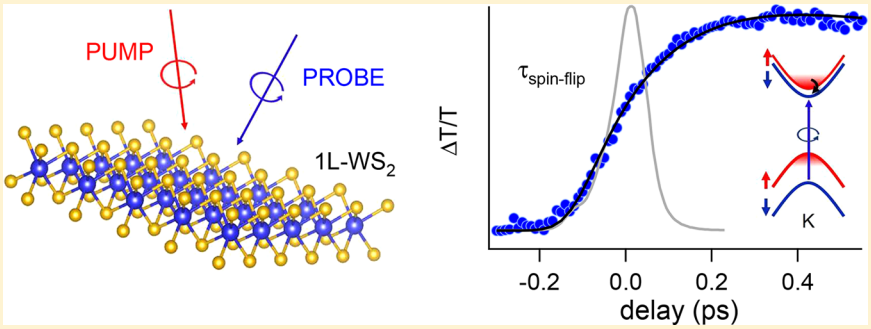

ABSTRACT: In monolayer (1L) transition metal dichalcogenides (TMDs) the valence and conduction bands are spin-split because of the strong spin−orbit interaction. In tungsten-based TMDs the spin-ordering of the conduction band is such that the so-called dark excitons, consisting of electrons and holes with opposite spin orientation, have lower energy than A excitons. The transition from bright to dark excitons involves the scattering of electrons from the upper to the lower conduction band at the K point of the Brillouin zone, with detrimental effects for the optoelectronic response of 1L-TMDs, since this reduces their light emission efficiency. Here, we exploit the valley selective optical selection rules and use two-color helicity-resolved pump−probe spectroscopy to directly measure the intravalley spin−flip relaxation dynamics in 1L-WS_2. This occurs on a sub-ps time scale, and it is significantly dependent on temperature, indicative of phonon-assisted relaxation. Time-dependent ab initio calculations show that intravalley spin−flip scattering occurs on significantly longer time scales only at the K point, while the occupation of states away from the minimum of the conduction band significantly reduces the scattering time. Our results shed light on the scattering processes determining the light emission efficiency in optoelectronic and photonic devices based on 1L-TMDs.

KEYWORDS: *Transition metal dichalcogenides, transient absorption spectroscopy, spin and valley dynamics, layered materials, optoelectronics*

Transition metal dichalcogenides (TMDs) are promising for optoelectronics,[1−4] valleytronics[5−9] and quantum information processing.[10] TMD monolayers (1L) are direct bandgap semiconductors,[11] with optical properties dominated by excitons with binding energies up to several hundred meVs.[12−18] The valence/conduction (VB/CB) band extrema lie at the nonequivalent K and K′ points at the edge of the Brillouin zone.[19,20] Their spin-degeneracy is lifted by strong spin−orbit (SO) interaction.[21] For the VB, the energy splitting, Δ_v, is between 150 and 400 meV,[22] while for the CB, Δ_c, it is 1−2 orders of magnitude lower (∼1−30 meV).[23,24] Together with a broken inversion symmetry, this results in spin-polarized bands and valley-dependent dipole-allowed interband optical transitions, as first detected by helicity resolved photoluminescence (PL).[25−27] The large VB splitting gives rise to two distinct interband transitions (called A and B) strongly renormalized by excitonic effects,[16] dominating the optical response in the visible range.[22]

References 28−33 predicted that, while the spin orientation of the upper and lower CB states is antiparallel in K/K′, in W-based 1L-TMDs, the upper CB has the same spin orientation as the upper VB. A consequence of this spin-ordering is the formation of an intravalley (i.e., zero momentum) dark exciton,

Received: July 7, 2018
Revised: September 8, 2018
Published: September 28, 2018

DOI: 10.1021/acs.nanolett.8b02774
Nano Lett. 2018, 18, 6882−6891

with a lower energy than the bright exciton. The bright to dark exciton transition reduces the PL quantum yield in W-based 1L-TMDs for decreasing temperatures.[33] The formation of dark excitons requires scattering processes such as intravalley relaxation.

Most experiments on TMDs focus on the study of intervalley scattering processes,[34−37] while intravalley ones are not yet well understood. References 38 and 39 suggested that intravalley scattering from the upper to the lower spin-split CB is one of the decay channels for the A exciton Kerr signal. However, based on the assumption that a spin−flip event occurs on a significantly longer time scale,[40−42] intravalley scattering is neglected in theoretical models describing exciton scattering in terms of electron−hole exchange interaction,[43] Dexter mechanism[44] (i.e., Coulomb-induced intervalley coupling between A and B excitons), and upconversion.[45]

Here, we present a combined experimental and theoretical study of intravalley scattering in 1L-WS_2. Exploiting two-color helicity-resolved pump−probe spectroscopy, we find an almost instantaneous buildup of the occupation of both CB states in the K′ valley after excitation of A-exciton transitions in the K valley. The buildup of the occupation of the lower CB state within the same valley is delayed, but still displays a short time constant ∼200 fs at 77 K. This becomes faster at higher temperatures, indicating phonon-mediated spin−flip scattering. This interpretation is confirmed by time-dependent ab initio calculations, where nonequilibrium many body perturbation theory (MBPT) is combined with density functional theory (DFT) to describe electron−electron and electron−phonon scattering. We show that the previously assumed long spin−flip processes occur only at the CB minimum. All excitation processes involving electronic states nearby the K point, e.g., induced by doping or by the finite bandwidth of the pump laser, decrease the scattering time. These results show that intravalley scattering occurs on a faster time scale than radiative recombination, indicating that dark excitons are the main reason for the very low (∼4%[46]) PL quantum yield of W-based 1L-TMDs, which determines the performance of optoelectronic and photonic devices based on these materials.[9]

1L-WS_2 flakes are produced by micromechanical cleavage from bulk WS_2 crystals (HQ Graphene). These are exfoliated with Nitto Denko tape, then further exfoliated on a polydimethylsiloxane (PDMS) stamp for inspection under an optical microscope and stamping on a 200 μm fused silica substrate, as described in ref 47. In order to facilitate the flakes' location, a metallic frame is fabricated around them by laser-writing, Cr/Au evaporation, and lift-off. The flakes are characterized by Raman spectroscopy (Figure 1a) using a Renishaw InVia spectrometer with a 100× objective and 514 nm excitation. In WS_2 the 2LA(M) mode at ∼352 cm^{-1}, due to the longitudinal acoustic phonons at the M point, overlaps with the E^1_{2g} mode,[48] requiring a multiple-Lorentzian fit to resolve them, Figure 1b. The intensity ratio of the 2LA(M) to the A_{1g} mode at 419 cm^{-1} is $I(2LA(M))/I(A_{1g})$ ∼ 4.6, consistent with 1L-WS_2.[48] Figure 1c shows the PL spectrum, with a single peak at ∼614 nm (∼2.02 eV). This originates from the A exciton. No light emission from the indirect gap, at an energy lower than the A exciton, is detected, confirming the 1L nature of the sample.[49]

Both equilibrium and nonequilibrium optical response of 1L-WS_2 are dominated by excitonic resonances.[22] To determine the position of these peaks, we perform broadband transient absorption measurements on an energy range

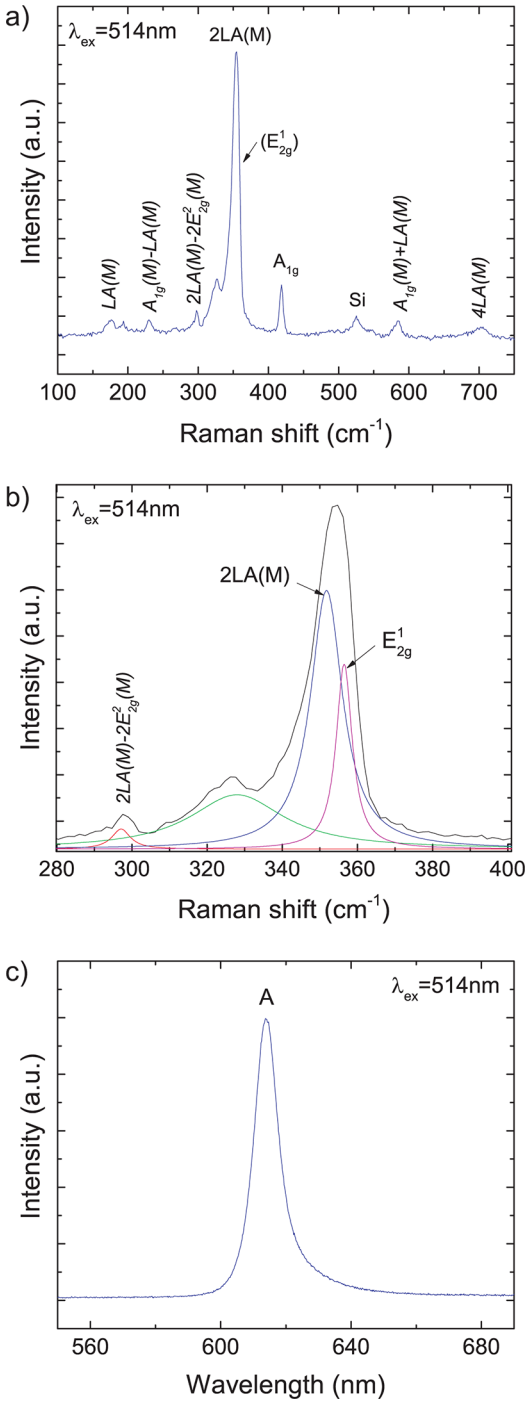

Figure 1. (a) Raman spectrum of 1L-WS_2 at 514 nm. (b) Multipeak fit. (c) PL spectrum of 1L-WS_2 at 514 nm. All measured at room temperature.

covering the visible spectrum. We use an amplified Ti:sapphire laser (Coherent Libra), emitting 100 fs pulses at 800 nm, with an average power ∼4 W at 2 kHz. Of this, ∼300 mW is used for the experiment. The output beam is divided by a splitter into two parts serving as a pump and probe. The pump is generated by a noncollinear optical parametric amplifier (NOPA) pumped by the second harmonic of the laser output, with a narrow band (10 nm), and tunable over the visible range (from 1.6 to 2.5 eV). The probe is obtained by white light continuum generation in a 2 mm sapphire plate. Pump and probe are collinearly focused on the sample with an

DOI: 10.1021/acs.nanolett.8b02774
Nano Lett. 2018, 18, 6882−6891

achromatic doublet. The pump pulse is modulated at 1 kHz by a mechanical chopper and, at the sample position, has a diameter ∼12 μm. After interaction with the sample, the probe is dispersed by a prism and is detected by a Si Charge Coupled Device (CCD) camera. The pump beam is linearly polarized, and it is tuned slightly above each of the A/B exciton peaks, while the white-light probe has perpendicular polarization and a spectral content covering both exciton transitions.

Figure 2 plots the differential transmission, $\Delta T/T$, spectra at different temporal delays. This shows positive peaks, centered

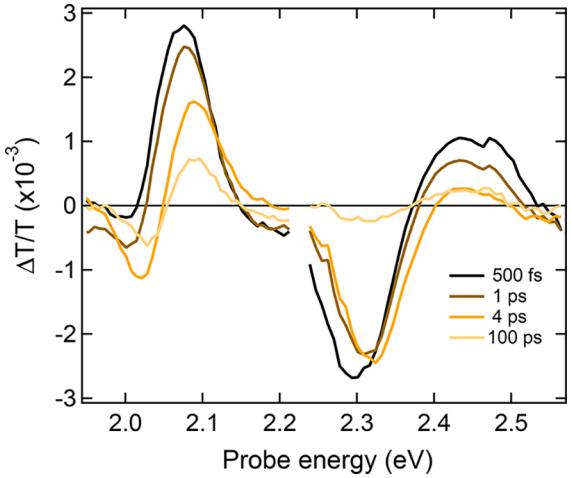

Figure 2. $\Delta T/T$ at different delay times around the A and B excitons at 77 K. Both pump and probe are linearly polarized. The pump energies are centred close the maxima of the A and B bleaching signals.

around the energies of the A/B excitons, due to photobleaching (PB) of the resonances, and red-shifted negative peaks, assigned to photoinduced absorption, as previously observed in other 1L-TMDs.[50−52] When the pump pulse induces an optical transition, phase-space filling, due to Pauli-blocking, reduces the absorption close to the band-edge. This induced transparency, as probed by the second pulse, results in PB. The photoinduced variation of the Coulomb screening of the electron−electron and electron−hole interactions renormalizes the quasi-particle band gap and the exciton binding energy, resulting in a transient redshift of the absorption edge,[53,54] which gives rise to the peculiar derivative shape of the transient spectra.[50] On a long time scale (>10 ps) transient heating, related to the scattering process between photoexcited carriers and phonon bath, further contributes to the non-equilibrium optical response.[53]

Henceforth, we will focus on the valley-resolved temporal dynamics on a narrow energy range, centered around the maximum of the A/B exciton bleaching signals. We perform two-color helicity-resolved transient absorption measurements with pump and probe beams both generated by NOPAs, in two different configurations. The pump beam is characterized by a central energy E_A = 2.09 eV and a bandwidth (30 meV) larger than the observed energy shift of the maximum of the A exciton PB (∼14 meV), reported in Figure 2, while the probe beam is either degenerate or nondegenerate with the pump (see Figure 3a). In the nondegenerate configuration, the probe is characterized by a central energy E_B = 2.45 eV and a bandwidth of 45 meV. The pump is modulated at 1 kHz (i.e., half of the laser repetition rate) by a mechanical chopper. Both beams are circularly polarized by a broadband quarter waveplate (B. Halle). After interaction with the sample, the probe beam is detected by a photodiode. The readout is then demodulated by a lock-in amplifier (Stanford SR830) enabling the detection of $\Delta T/T$ down to $\sim 10^{-4}$.

The spin ordering of the CB states in 1L-WS_2 is such that the pump excites electrons from the upper VB to the upper CB. The photogenerated holes are not expected to scatter into the lower VB within the time scale of our experiment because the energy splitting of the VB in K is over 1 order of magnitude higher than the CB splitting. Therefore, it is more likely for photoexcited electrons to lose energy and scatter from upper to lower CB states, than for holes to gain energy and scatter from the upper to lower VB states in K, consequently blocking the absorption of the probe beam around the B exciton transition. Reference 55 showed that the spin−flip process for holes in 1L-TMDs at 77 K occurs through the Elliott−Yafet mechanism on a time scale ∼10 ns, i.e., 4−5 orders of magnitude longer than the sub-ps time scale of our experiments. Thus, in the degenerate configuration, the probe is sensitive to the decay of the excited electron population in the upper CB. In the nondegenerate configuration, the probe measures the electron population in the lower CB, which is related to the dark excitons. With left- (right-) circular polarized light, we can access the K (K′) valley because of the optical selection rules. This enables us to disentangle the intra- and intervalley scattering processes. To study the intravalley relaxation dynamics, both pump and probe have the same helicity.

Figure 3b plots the transient absorption signal for the degenerate (red curve, $\Delta T/T_{A,K}$) and nondegenerate (blue curve, $\Delta T/T_{B,K}$) configuration. The positive sign of both curves corresponds to the PB of the A and B transitions. The $\Delta T/T_{A,K}$ trace exhibits a pulse-width limited build-up, followed by a relaxation dynamics fitted by a double exponential with decay times τ_A^{fast} = 150 ± 10 fs and τ_A^{slow} = 4.5 ± 0.5 ps. $\Delta T/T_{B,K}$ has a single exponential decay with τ_B = 5 ± 0.5 ps and reaches its maximum at a delayed time with respect to the pump excitation, Figure 3c. The rise time τ_{rise} = 210 ± 10 fs is estimated by fitting the build-up dynamics with the function $1 - \exp(-t/\tau_{rise})$ convoluted with a Gaussian instrumental response function (IRF), obtained by sum-frequency cross-correlation experiments between pump and probe pulses, accounting for the temporal resolution ∼100 fs.

The instantaneous rise of $\Delta T/T_{A,K}$ is interpreted as a phase space filling of the final state by Pauli blocking and transient optical gap renormalization. The latter is caused by the transient change of the Coulomb screening and has a characteristic time scale (∼tens of fs[56]) much faster than the temporal resolution of our setup. Therefore, the finite buildup of the PB signal around the B exciton can only arise from Pauli blocking, due to the scattering of the carriers from the upper to the lower CB at K.

Many scattering mechanisms contribute to the depletion of the bright state on a sub-ps time scale, since bright excitons can radiatively recombine in the same valley,[35] scatter into the opposite valley,[34,36,37,44,45] or form dark excitons with nonzero momentum.[57] It is often assumed that direct intravalley scattering, requiring a spin−flip, occurs on times >10 ps.[40−42,58−60] However, our data suggest that this process might be much faster. We find that $\tau_A^{fast} \sim$ 150 fs is very close to $\tau_{rise} \sim$ 210 fs. Therefore, τ_{rise} can be associated with intravalley scattering.

DOI: 10.1021/acs.nanolett.8b02774
Nano Lett. 2018, 18, 6882−6891

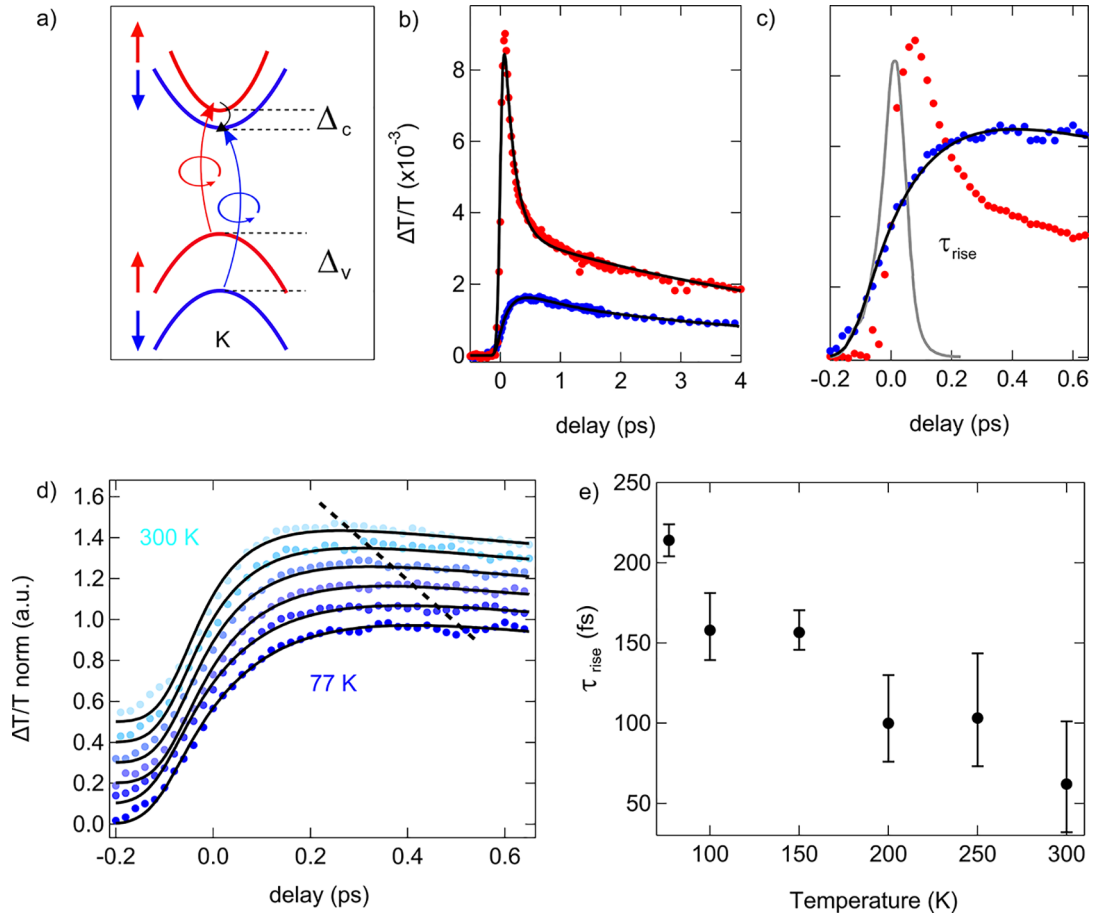

Figure 3. Spin-flip relaxation process. (a) A excitons are injected in the K valley by a circularly polarized pump (red arrow). The probe pulse has the same helicity, and it is resonant with the B exciton (blue arrow). The gradual filling of the lower CB states due to intravalley scattering hinders the absorption of the probe by Pauli blocking, causing a delayed formation of the bleaching signal around the B exciton. (b) Red and blue curves are $\Delta T/T$ at 77 K around the A and B transitions. The pump fluence is ~70 μJ/cm^2. (c) Close up at shorter delay time of the transient optical response. The blue trace is multiplied by 4 to highlight the different build-up dynamics. For the same pump and probe energies, the build-up dynamics is pulsewidth limited, while the nondegenerate configuration displays a delayed formation. The gray line is the cross correlation between pump and probe pulses. The black line is a fit to the data. (d) $\Delta T/T_{B,K}$ at different temperatures. The dashed line through the maximum of each trace highlights the increasing rate of intravalley scattering at higher temperatures. The solid black lines are obtained by fitting the rising edge of the $\Delta T/T$ traces with an exponential convoluted with the IRF, as discussed in the main text. (e) Temperature dependence of τ_{rise}, as obtained from the fits in (d). The error bars are derived from the fit of $\Delta T/T$ in (d).

To gain a deeper insight into the underlying scattering mechanism, we study the temperature dependence of $\Delta T/T_{B,K}$, Figure 3d. The rise time significantly decreases at higher temperatures, Figure 3e. This suggests that intravalley spin relaxation between upper and lower CB is phonon-assisted. Among all first order phonon scattering processes, only phonons with a momentum close to zero (around Γ) can play a role. The Γ, in-plane, Raman-active, optical phonons with symmetry Γ_5 at ~285 cm^{-1} are good candidates for mediating such a scattering process within the same valley because their energy (~35 meV) is very close to that of the spin splitting in the CB.[61,62] Long wavelength flexural phonons have been considered, but the associated relaxation dynamics is orders of magnitude longer than in our measurements.[40,58]

Figure 4 compares the $\Delta T/T_{B,K}$ build-up dynamics at different photoinduced carrier densities between ~10^{12} and 10^{13} cm^{-2}. This shows no variation of build-up and decay dynamics. This provides important information on the origin of the spin−flip scattering. Since only electron−electron or Auger scattering are expected to depend on the number of photoexcited carriers, we neglect this process as the main mechanism driving the spin relaxation between upper and lower CB states. Since intravalley relaxation is a transition of

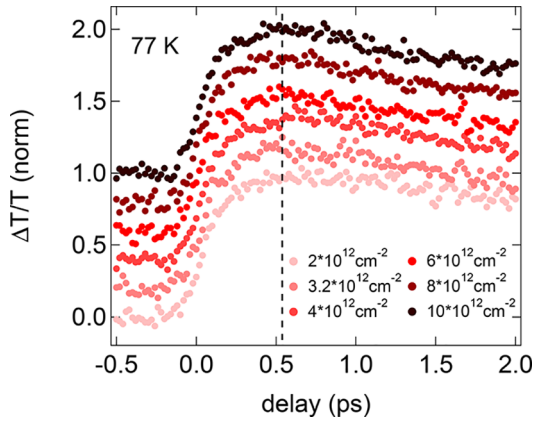

Figure 4. Normalized $\Delta T/T$ around the B exciton in 1L-WS_2 at 77 K for different photoinduced carrier densities. The curves are offset for better legibility.

DOI: 10.1021/acs.nanolett.8b02774
Nano Lett. 2018, 18, 6882−6891

electrons from the upper to the lower CB, we expect the scattering time to depend on Δ_c, which, for 1L-WS_2, is estimated to be ~26 meV (see inset of the band structure in Figure 10a). This is substantiated by performing the same experiments on 1L-MoS_2. Here the spin ordering of the CB state at K is reversed compared to 1L-WS_2, implying that the bright exciton has lower energy than the dark one.[23]

Reference 23 reported that in 1L-MoS_2 chalcogen and metal atoms contributions to the CB splitting have opposite signs and almost cancel each other, resulting in a very small CB splitting (~3 meV[23]) when compared to other 1L-TMDs. Figure 5 plots the transient optical response around the A (E_A = 1.85 eV) and B (E_B = 2.05 eV) excitons of 1L-MoS_2 (red and blue curves respectively) after spin-polarized carriers are photoinjected in the K valley by a 100 fs pump pulse in resonance with the A exciton. Unlike 1L-WS_2, both $\Delta T/T$ traces have the same pulse width-limited build up dynamics. This shows that intravalley spin−flip scattering is more efficient for 1L-MoS_2 than 1L-WS_2. This confirms the trend suggested by the calculations of ref 40 whereby, despite the lower SO splitting, Mo-based 1L-TMDs have faster spin relaxation time than W-based 1L-TMDs, and further supports the interpretation that τ_{rise} is a direct measurement of the intravalley scattering time.

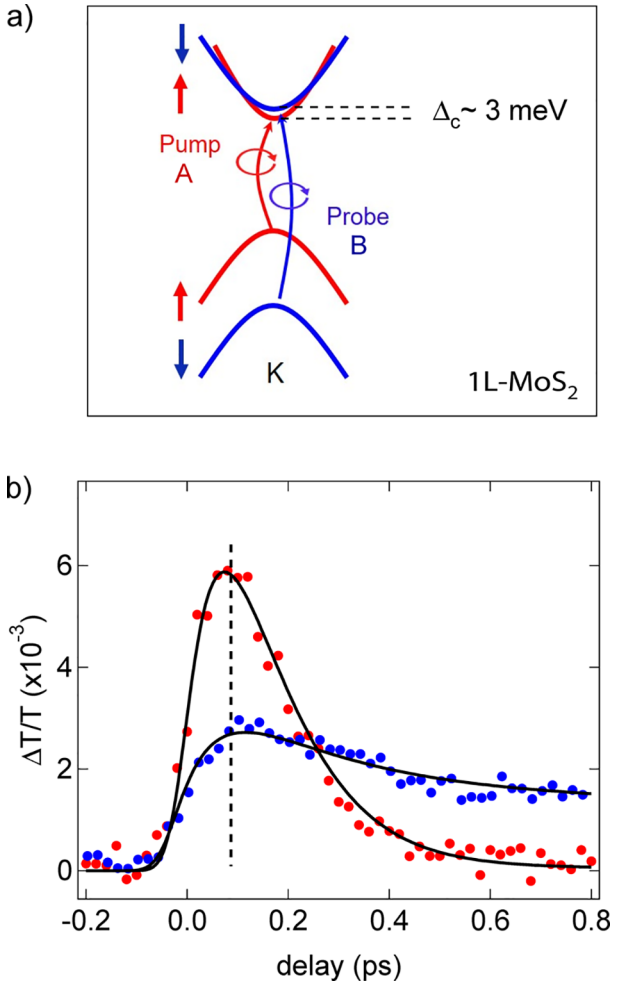

Figure 5. (a) 1L-MoS_2 band structure around K. (b) $\Delta T/T$ around the A (red curve) and B (blue curve) excitons at 77 K. The incident pump fluence is the same as that for the $\Delta T/T$ measurements on 1L-WS_2 in Figure 3. The continuous lines are fit to the data. Both traces have the same build up time, as indicated by the dashed line.

In 1L-WS_2, in addition to intravalley relaxation, scattering into the opposite valley is expected to be a major channel for the depletion of the A excitons at K.[34,36,37,44,45] We address this by switching the probe to the opposite helicity. We measure the transient absorption in the K′ valley around the A ($\Delta T/T_{A,K'}$) and B ($\Delta T/T_{B,K'}$) transitions, Figure 6a,b. Figure 6c compares $\Delta T/T_{A,K'}$ (pink) to the previously discussed instantaneous build-up in $\Delta T/T_{A,K}$. We get τ_{rise} = 30 ± 10 fs. This fast time scale is consistent with the high-temporal resolution time-resolved photoemission experiments of ref 63, confirming the strong coupling between K and K′. The valley polarization is defined as the imbalance of the exciton population between K and K′: $\Delta T/T_{A,K} - \Delta T/T_{A,K'}$.

The A polarization (green line in Figure 6c) drops by a factor 10 within the first ~500 fs, followed by a slower decay within a few ps, in agreement with previous measurements on 1L-MoS_2[34] and 1L-WS_2.[44] This fast depolarization was previously explained by electron−hole exchange interaction[45,64,65] and Coulomb-induced[66] or phonon-mediated[67] intervalley scattering. Valley polarization is also limited by intravalley scattering, which manifests on the sub-ps time scale.

Figure 6d compares the measurements of the B transition in the two valleys. The rise time in the unpumped valley is 90 ± 20 fs. Despite the large momentum mismatch, both $\Delta T/T_{A,K'}$ and $\Delta T/T_{B,K'}$ have a faster build-up than $\Delta T/T_{B,K}$. The valley polarization of the B exciton (green curve) shows a sign change, previously observed in ref 44 and assigned to slightly different time scales of inter- and intravalley scattering.

To validate our conclusions, we perform time-dependent ab initio calculations using a first-principles implementation of nonequilibrium MBPT.[68−73] We use the Quantum Espresso suite[74] to compute the equilibrium properties of 1L-WS_2. The static absorption and the band structure of 1L-WS_2 are calculated using equilibrium MBPT on top of DFT, within the local density approximation (LDA), by taking into account the strong SO interaction. Figure 7 plots the calculated electronic bands along Γ-*K*-*M* and Γ-*K*′-*M*. Figure 8 plots the computed optical spectrum where both GW corrections in the quasi-particle energy and SO interactions, with full spinor wave functions, are included. We use a 24 × 24 × 1 **k**-grid to calculate the Bethe−Salpeter kernel. The eigenvalues and spinorial wave functions are calculated with 110 Ry cutoff and a 15 × 15 × 1 **k**-point mesh. The position of the A exciton determines the theoretical pump energy to mimic the experiments, where the pump is set to be resonant with A. The phonon density of states (PDOS) of 1L-WS_2 is calculated using Density Functional Perturbation Theory (DFPT) as implemented in Quantum Espresso,[61] Figure 9. The calculated quasi-particle band structure has a direct gap at K where the VB and CB SO splitting are Δ_v ~ 455 meV and Δ_c ~ 26 meV, as shown in Figure 10a. We consider the last two VBs and the first two CBs to describe the carrier dynamics. Electron−phonon matrix elements are computed within DFPT. The real-time simulation is performed with the Yambo code.[75] The dynamics as a function of the pump−probe delay τ is obtained by solving the Kadanoff−Baym equation for the one-body density matrix ρ, within the Generalized Kadanoff−Baym ansatz:[68,69]

$$\partial_t \rho(\tau) = \partial_t \rho(\tau)_{coh} + \partial_t \rho(\tau)_{coll} \quad (1)$$

DOI: 10.1021/acs.nanolett.8b02774
Nano Lett. 2018, 18, 6882−6891

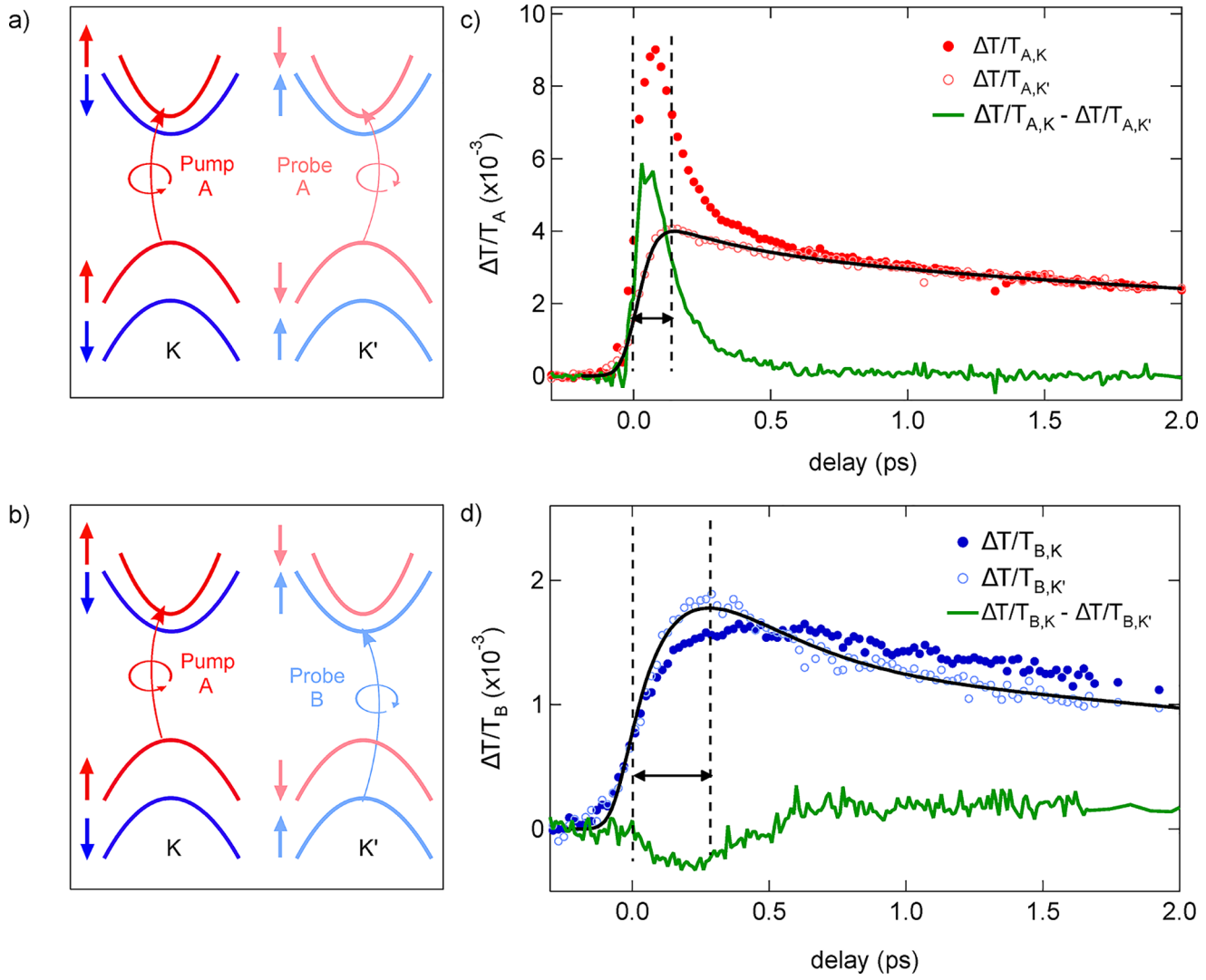

Figure 6. Intervalley relaxation dynamics in 1L-WS_2. (a,b) Intervalley scattering processes. The K′ bands have opposite spin orientation and are depicted with lighter colors. (c,d) Temporal dynamics by photoexciting A excitons at K and measuring $\Delta T/T$ at K and K′ at the A and B resonances at 77 K. The green lines are differences between signals with the same and opposite polarizations. They are directly related to the valley depolarization dynamics. The dashed lines are centered at zero delay and at the maximum of the $\Delta T/T$ in K′.

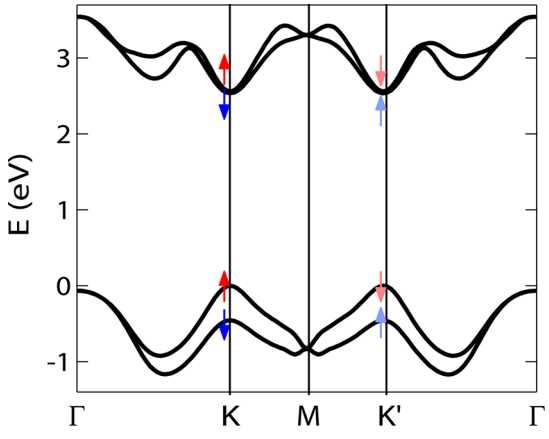

Figure 7. Band structure of 1L-WS_2. Arrows mark the direction of the z-component of the spin for the CB and VB edges at K and K′.

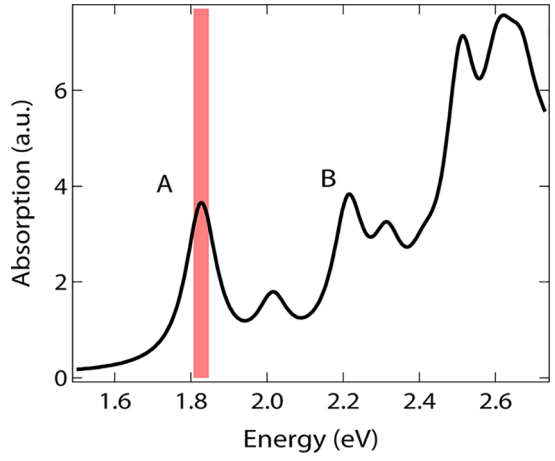

Figure 8. Absorption of 1L-WS_2 from the Bethe−Salpeter equation. The A and B excitons are indicated. The pump energy is marked with a red band.

The coherent term, $\partial_t \rho(\tau)_{\mathrm{coh}}$, includes the electron−hole interaction experienced by the photoexcited electron−hole pairs and describes the interaction with the pump laser, while

DOI: 10.1021/acs.nanolett.8b02774
Nano Lett. 2018, 18, 6882−6891

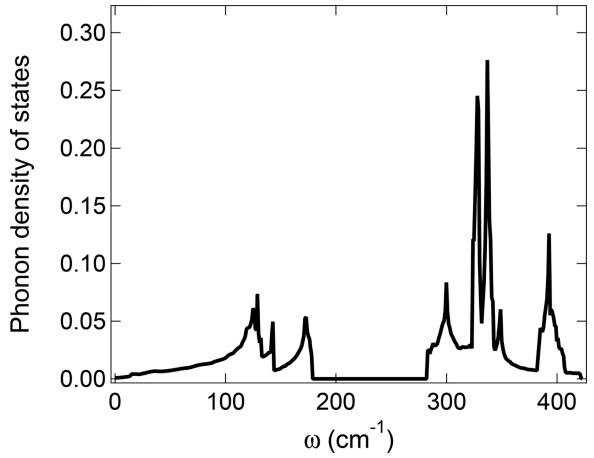

Figure 9. PDOS of 1L-WS_2. The frequency gap between low and high phonon modes is ∼110 cm^{-1}. At low frequencies, the PDOS is characterized by two peaks, while at high energy it is dominated by a peak at ∼340 cm^{-1}, associated with the E′ mode at Γ.

the dissipative term, $\partial_t \rho(\tau)_{coll}$, accounts for all scattering processes. The equation of motion for the density matrix is projected on four bands $\rho_{nm\mathbf{k}}$. The real-time simulation adopts a coarse 24 × 24 × 1 and a denser 61 × 61 × 1 **k**-grid. This is performed on the denser grid with matrix elements and density matrix interpolated (by using a nearest neighbor technique) from the coarse grid. The experimental pump pulse is simulated by using a narrow band pump centered at the computed A-exciton position (intensity ∼ 10^4kW/m^2; full width at half maximum ∼ 100 fs, energy ∼ 1.85 eV). The screened-exchange approximation, together with a quasi-particle shift ∼1.039 eV guarantee that the pump is absorbed at the excitonic peak.[70] The nonequilibrium population, $f_i(\tau)$, is defined as the diagonal part of the single-particle density matrix $f_i(\tau) = \rho_{ii}(\tau)$, with i the generic index representing the electronic band and momentum. By solving eq 1, we access the carrier distribution for all momenta and bands at different τ. The carriers are selectively photoexcited in the K valley by a circularly polarized pump pulse centered around the A exciton. The inset of Figure 10b is the computed photoexcited CB electron distribution for each Brillouin zone point for τ = 0 (i.e., the maximum of the pump pulse temporal profile). This

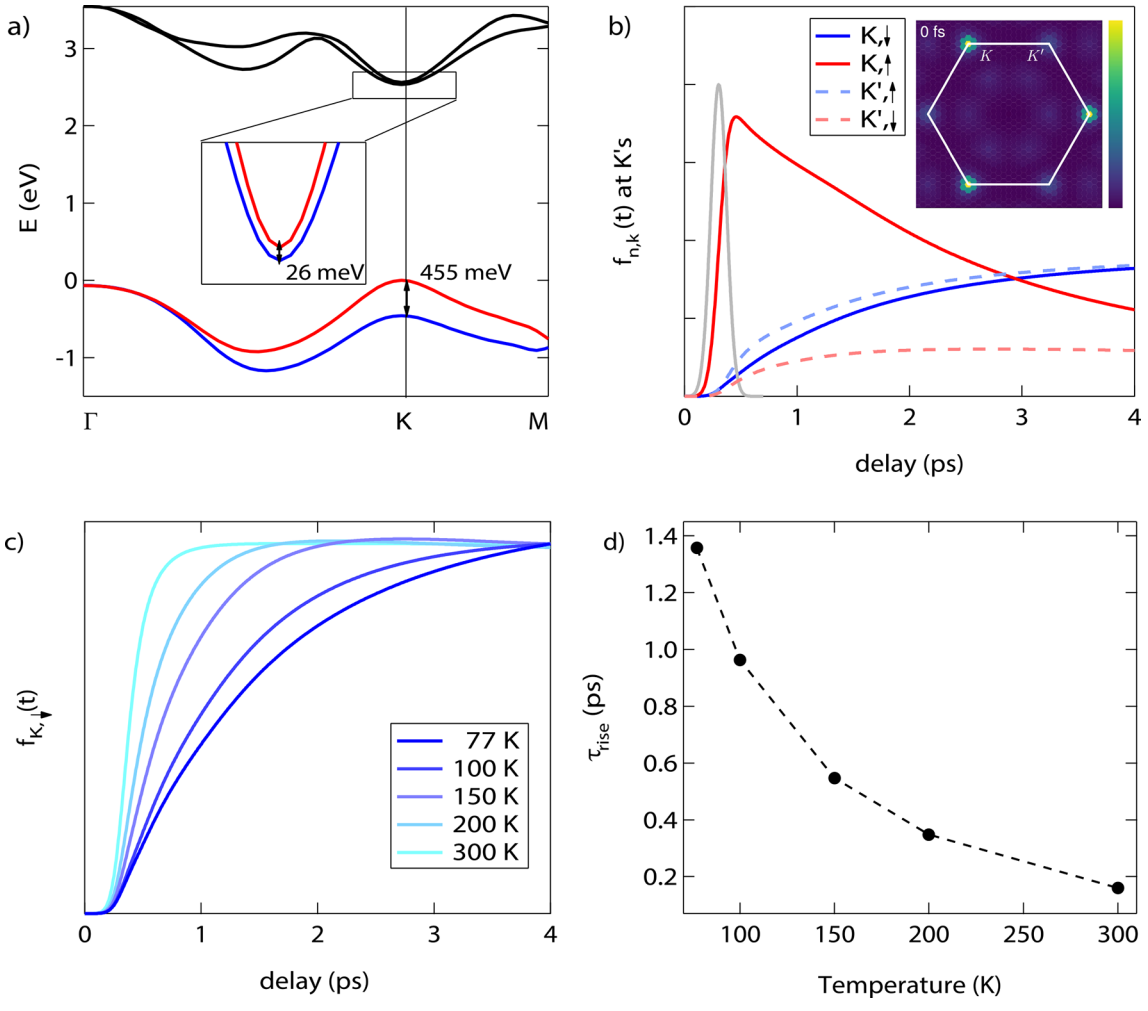

Figure 10. (a) 1L-WS_2 band structure. The red and blue colors corresponds to S_z = ↑ and S_z = ↓. The inset is a close-up of the spin-split CB around K. (b) Time evolution of the carrier population in the (K,↓) (K,↑), (K′,↑) and (K′,↓) states, simulated at 77 K. The inset depicts the carrier distribution at zero pump−probe delay projected on the K,K′ momentum plane. At τ = 0, the K valleys concentrate most on the electron population. (c) Time evolution of the (K,↓) population as a function of temperature. (d) Rise times obtained by fitting the traces in (c) by an exponential convoluted with a 100 fs Gaussian response function.

DOI: 10.1021/acs.nanolett.8b02774
Nano Lett. 2018, 18, 6882−6891

confirms the valley selectivity by circular polarization. The temporal evolution of the system out of equilibrium is governed by the collision term in eq 1, including electron−electron and electron−phonon scattering. Since we have not measured any appreciable variation of the intravalley dynamics for different excitation fluence (Figure 4), we include in $\partial_t \rho(\tau)_{\text{coll}}$ only the electron−phonon scattering channel and disregard electron−electron scattering. Our assumption is also supported by ref 72, where intervalley scattering in 1L-WSe_2 was well described in terms of electron−phonon scattering.

We focus only on the temporal evolution of the occupation $f_i(\tau)$ for the 4 CB states with opposite spin orientation at K/K′; (K;↑), (K;↓), (K′;↑), and (K′;↓) (Figure 6a). The population is first injected in (K;↑) and then scattered toward the other three states by phonon-mediated processes. The dynamics of $f_{(K;\downarrow)}(\tau)$ (blue trace in Figure 10b) is governed by phonon-mediated spin−flip intravalley scattering. The time scale of the simulated build-up dynamics reproduces our experiments, unlike refs 40 and 41. The small discrepancy between calculations and experiments is due to the fact that other processes, such as exchange interaction[64] and the Dexter mechanism,[44] are not taken into account, due to the high computational cost. The corresponding τ_{rise} of $f_{(K;\downarrow)}(\tau)$ decreases at higher temperature as a consequence of the larger phonon population, widening the range of scattering channels available, Figure 10c,d. The $f_{(K';\downarrow)}(\tau)$ and $f_{(K';\uparrow)}(\tau)$ dynamics are related to phonon-mediated intervalley scattering for photoexcited electrons in CB (red and blue dashed curves). In this case, the larger electron−phonon matrix elements make the spin-conserving (K;↑) → (K′;↑) transition faster, even though it involves large momentum phonons. Nevertheless, the scattering toward (K;↓) has a similar fast τ_{rise} since (K;↓) is the lowest energy state where carriers accumulate.

Our calculations demonstrate that inter- and intravalley scattering are driven by phonon-mediated processes. Nevertheless, K → K′ transitions of carriers located *exactly* at the bands minimum/maximum are very slow.[76] However, this does not contradict our results. The electron−phonon matrix elements, evaluated between these states at K and K′, which correspond to a complete spin flip, are zero. Therefore, the K → K′ dynamics of such localized carriers is much slower that the dynamics observed experimentally. This apparent discrepancy is reconciled by observing that the carriers are distributed *around* K and K′, due to the finite laser energy bandwidth, the broadening of the states (proportional to the density of states) caused by quasi-particle corrections[18] and the fast intravalley scattering that tends to equilibrate carries in the valley by creating a Fermi−Dirac distribution with a finite temperature. Thus, the inter and intravalley dynamics in Figure 10b are caused by the scattering of carriers around K and K′. The strength of the interaction and the speed of the transitions are dictated by the density of carriers around the band minima/maxima.

Our simulations predict build-up times of $f_i(\tau)$ slower than the measured $\Delta T/T$. This can be explained by phenomena not included in our calculations, like the pump-induced optical gap renormalization or the Dexter mechanism.[44] In order to include the optical gap renormalization effect, the temporal evolution of the nonequilibrium optical spectrum has to be simulated. In ref 50 we have done this by computing the nonequilibrium carrier population created by the pump pulse and the additional Coulomb screening caused by the modification of the electronic occupations. However, this is restricted to a single time delay.[50] For an extended temporal range (i.e., the first few ps after pump excitation) this becomes computationally extremely demanding. At present, the Dexter mechanism has only been implemented with semiempirical approaches, selecting, ad hoc, the exciton states participating in the dynamics.[44] A nonequilibrium ab initio formalism including the Dexter mechanism has not been developed yet. Despite this, the electron−phonon interaction remains the driving mechanism, which explains the experimental temperature dependence.

In conclusion, we studied intra- and intervalley relaxation dynamics in 1L-WS_2 by two-color helicity-resolved transient absorption spectroscopy. This allowed us to separately probe and disentangle these processes. Intravalley relaxation is fast (<1 ps), leading to a very efficient depletion of the bright A exciton. The temperature dependence of the intravalley scattering rate is a signature of a phonon-mediated process, which depends on the value of the CB spin splitting. Ab initio simulations are in good agreement with experiments, confirming the fast time scale. The valley polarization in 1L-WS_2 has a similarly fast relaxation time, suggesting a strong interaction between the two valleys. We stress that, since intravalley spin−flip and intervalley scattering processes are effective on the same time scale, the former relaxation mechanism cannot be disregarded in explaining the fast valley depolarization of A excitons in 1L-WS_2. Since the intravalley scattering process determines the formation of the dark intravalley exciton, our results indicate that the bright to dark intravalley exciton transition occurs on a sub-ps time scale.

Our work has implications for the emerging fields of valleytronics and optoelectronics with layered semiconductors because it demonstrates that, unlike previous assumptions, intravalley spin−flip scattering is an efficient decay channel for valley polarization. Our results clarify the mechanisms leading to fast degradation of the valley polarization in TMDs and, at the same time, shed light on the scattering processes that determine the light emission efficiency in optoelectronic and photonic devices based on 1L-TMDs, such as light emitting diodes[77] and polarized photon emitters.[78]

AUTHOR INFORMATION

Corresponding Author

*E-mail: acf26@eng.cam.ac.uk. Phone: +44-1223-748351. Fax: +44-1223-748348.

ORCID

Alejandro Molina-Sánchez: 0000-0001-5121-4058
Davide Sangalli: 0000-0002-4268-9454
Andrea C. Ferrari: 0000-0003-0907-9993
Giulio Cerullo: 0000-0002-9534-2702
Stefano Dal Conte: 0000-0001-8582-3185

Author Contributions

#Z.W., A. M.S., and P.A. contributed equally to this work.

Notes

The authors declare no competing financial interest.

ACKNOWLEDGMENTS

We thank Andreas Knorr, Mikhail Glazov, Alexey Chernikov, and Ivan Bernal-Villamil for useful discussions. We acknowledge funding from the National Research Fund, Luxembourg (Projects C14/MS/773152/FAST-2DMAT and INTER/ANR/13/20/NANOTMD), the Juan de la Cierva Program,

DOI: 10.1021/acs.nanolett.8b02774
Nano Lett. 2018, 18, 6882−6891

the EU Graphene Flagship, ERC grant Hetero2D, EPSRC grants EP/L016087/1, EP/K01711X/1, EP/K017144/1, the Early Postdoc Mobility program of the Swiss National Science Foundation (P2BSP2 168747), the EU project MaX Materials design at the eXascale H2020-EINFRA-2015-1, and Nanoscience Foundries and Fine Analysis-Europe H2020-INFRAIA-2014-2015.

REFERENCES

(1) Wang, Q. H.; Kalantar-Zadeh, K.; Kis, A.; Coleman, J. N.; Strano, M. S. *Nat. Nanotechnol.* **2012**, *7*, 699−712.
(2) Koppens, F. H. L.; Mueller, T.; Avouris, P.; Ferrari, A. C.; Vitiello, M. S.; Polini, M. *Nat. Nanotechnol.* **2014**, *9*, 780−793.
(3) Mak, K. F.; Shan, J. *Nat. Photonics* **2016**, *10*, 216−226.
(4) Ferrari, A. C.; Bonaccorso, F.; Fal'ko, V.; Novoselov, K. S.; Roche, S.; Boggild, P.; Borini, S.; Koppens, F. H. L.; Palermo, V.; Pugno, N.; et al. *Nanoscale* **2015**, *7*, 4598−4810.
(5) Yuan, H.; Wang, X.; Lian, B.; Zhang, H.; Fang, X.; Shen, B.; Xu, G.; Xu, Y.; Zhang, S.-C.; Hwang, H. Y.; et al. *Nat. Nanotechnol.* **2014**, *9*, 851−857.
(6) Yao, W.; Xiao, D.; Niu, Q. *Phys. Rev. B: Condens. Matter Mater. Phys.* **2008**, *77*, 235406.
(7) Aivazian, G.; Gong, Z.; Jones, A. M.; Chu, R.-L.; Yan, J.; Mandrus, D. G.; Zhang, C.; Cobden, D.; Yao, W.; Xu, X. *Nat. Phys.* **2015**, *11*, 148−152.
(8) Ye, Y.; Xiao, J.; Wang, H.; Ye, Z.; Zhu, H.; Zhao, M.; Wang, Y.; Zhao, J.; Yin, X.; Zhang, X. *Nat. Nanotechnol.* **2016**, *11*, 598−602.
(9) Schaibley, J. R.; Yu, H.; Clark, G.; Rivera, P.; Ross, J. S.; Seyler, K. L.; Yao, W.; Xu, X. *Nat. Rev. Mater.* **2016**, *1*, 16055.
(10) Srivastava, A.; Sidler, M.; Allain, A. V.; Lembke, D. S.; Kis, A.; Imamoglu, A. *Nat. Nanotechnol.* **2015**, *10*, 491−496.
(11) Mak, K. F.; Lee, C.; Hone, J.; Shan, J.; Heinz, T. F. *Phys. Rev. Lett.* **2010**, *105*, 136805.
(12) Chernikov, A.; Berkelbach, T. C.; Hill, H. M.; Rigosi, A.; Li, Y.; Aslan, O. B.; Reichman, D. R.; Hybertsen, M. S.; Heinz, T. F. *Phys. Rev. Lett.* **2014**, *113*, 076802.
(13) Ugeda, M. M.; Bradley, A. J.; Shi, S.-F.; da Jornada, F. H.; Zhang, Y.; Qiu, D. Y.; Ruan, W.; Mo, S.-K.; Hussain, Z.; Shen, Z.-X.; et al. *Nat. Mater.* **2014**, *13*, 1091−1095.
(14) Zhu, B.; Chen, X.; Cui, X. *Sci. Rep.* **2015**, *5*, 9218.
(15) Komsa, H.-P.; Krasheninnikov, A. V. *Phys. Rev. B: Condens. Matter Mater. Phys.* **2012**, *86*, 241201.
(16) Qiu, D. Y.; da Jornada, F. H.; Louie, S. G. *Phys. Rev. Lett.* **2013**, *111*, 216805.
(17) Molina-Sánchez, A.; Hummer, K.; Wirtz, L. *Surf. Sci. Rep.* **2015**, *70*, 554−586.
(18) Molina-Sánchez, A.; Palummo, M.; Marini, A.; Wirtz, L. *Phys. Rev. B: Condens. Matter Mater. Phys.* **2016**, *93*, 155435.
(19) Zhang, Y.; Chang, T.-R.; Zhou, B.; Cui, Y.-T.; Yan, H.; Liu, Z.; Schmitt, F.; Lee, J.; Moore, R.; Chen, Y.; et al. *Nat. Nanotechnol.* **2014**, *9*, 111−115.
(20) Splendiani, A.; Sun, L.; Zhang, Y.; Li, T.; Kim, J.; Chim, C.-Y.; Galli, G.; Wang, F. *Nano Lett.* **2010**, *10*, 1271−1275.
(21) Molina-Sánchez, A.; Sangalli, D.; Hummer, K.; Marini, A.; Wirtz, L. *Phys. Rev. B: Condens. Matter Mater. Phys.* **2013**, *88*, 045412.
(22) Li, Y.; Chernikov, A.; Zhang, X.; Rigosi, A.; Hill, H. M.; van der Zande, A. M.; Chenet, D. A.; Shih, E.-M.; Hone, J.; Heinz, T. F. *Phys. Rev. B: Condens. Matter Mater. Phys.* **2014**, *90*, 205422.
(23) Kośmider, K.; González, J. W.; Fernández-Rossier, J. *Phys. Rev. B: Condens. Matter Mater. Phys.* **2013**, *88*, 245436.
(24) Kormányos, A.; Zólyomi, V.; Drummond, N. D.; Burkard, G. *Phys. Rev. X* **2014**, *4*, 011034.
(25) Mak, K. F.; He, K.; Shan, J.; Heinz, T. F. *Nat. Nanotechnol.* **2012**, *7*, 494−498.
(26) Cao, T.; Wang, G.; Han, W.; Ye, H.; Zhu, C.; Shi, J.; Niu, Q.; Tan, P.; Wang, E.; Liu, B.; et al. *Nat. Commun.* **2012**, *3*, 887.
(27) Zeng, H.; Dai, J.; Yao, W.; Xiao, D.; Cui, X. *Nat. Nanotechnol.* **2012**, *7*, 490−493.
(28) Yu, H.; Cui, X.; Xu, X.; Yao, W. *National Science Review* **2015**, *2*, 57−70.
(29) Baranowski, M.; Surrente, A.; Maude, D. K.; Ballottin, M.; Mitioglu, A. A.; Christianen, P. C. M.; Kung, Y. C.; Dumcenco, D.; Kis, A.; Plochocka, P. *2D Mater.* **2017**, *4*, 025016.
(30) Slobodeniuk, A. O.; Basko, D. M. *2D Mater.* **2016**, *3*, 035009.
(31) Zhang, X.-X.; Cao, T.; Lu, Z.; Lin, Y.-C.; Zhang, F.; Wang, Y.; Li, Z.; Hone, J. C.; Robinson, J. A.; Smirnov, D.; et al. *Nat. Nanotechnol.* **2017**, *12*, 883−888.
(32) Molas, M. R.; Faugeras, C.; Slobodeniuk, A. O.; Nogajewski, K.; Bartos, M.; Basko, D. M.; Potemski, M. *2D Mater.* **2017**, *4*, 021003.
(33) Zhang, X.-X.; You, Y.; Zhao, S. Y. F.; Heinz, T. F. *Phys. Rev. Lett.* **2015**, *115*, 257403.
(34) Dal Conte, S.; Bottegoni, F.; Pogna, E. A. A.; De Fazio, D.; Ambrogio, S.; Bargigia, I.; D'Andrea, C.; Lombardo, A.; Bruna, M.; Ciccacci, F.; et al. *Phys. Rev. B: Condens. Matter Mater. Phys.* **2015**, *92*, 235425.
(35) Zhu, C. R.; Zhang, K.; Glazov, M.; Urbaszek, B.; Amand, T.; Ji, Z. W.; Liu, B. L.; Marie, X. *Phys. Rev. B: Condens. Matter Mater. Phys.* **2014**, *90*, 161302.
(36) Mai, C.; Semenov, Y. G.; Barrette, A.; Yu, Y.; Jin, Z.; Cao, L.; Kim, K. W.; Gundogdu, K. *Phys. Rev. B: Condens. Matter Mater. Phys.* **2014**, *90*, 041414.
(37) Mai, C.; Barrette, A.; Yu, Y.; Semenov, Y. G.; Kim, K. W.; Cao, L.; Gundogdu, K. *Nano Lett.* **2014**, *14*, 202−206.
(38) Plechinger, G.; Nagler, P.; Arora, A.; Schmidt, R.; Chernikov, A.; del Águila, A. G.; Christianen, P. C. M.; Bratschitsch, R.; Schüller, C.; Korn, T. *Nat. Commun.* **2016**, *7*, 12715.
(39) Plechinger, G.; Korn, T.; Lupton, J. M. *J. Phys. Chem. C* **2017**, *121*, 6409−6413.
(40) Song, Y.; Dery, H. *Phys. Rev. Lett.* **2013**, *111*, 026601.
(41) Ochoa, H.; Roldán, R. *Phys. Rev. B: Condens. Matter Mater. Phys.* **2013**, *87*, 245421.
(42) Wang, L.; Wu, M. W. *Phys. Rev. B: Condens. Matter Mater. Phys.* **2014**, *89*, 115302.
(43) Glazov, M. M.; Amand, T.; Marie, X.; Lagarde, D.; Bouet, L.; Urbaszek, B. *Phys. Rev. B: Condens. Matter Mater. Phys.* **2014**, *89*, 201302.
(44) Berghäuser, G.; Bernal-Villamil, I.; Schmidt, R.; Schneider, R.; Niehues, I.; Erhart, P.; Michaelis de Vasconcellos, S.; Bratschitsch, R.; Knorr, A.; Malic, E. *Nat. Commun.* **2018**, *9*, 971.
(45) Manca, M.; Glazov, M. M.; Robert, C.; Cadiz, F.; Taniguchi, T.; Watanabe, K.; Courtade, E.; Amand, T.; Renucci, P.; Marie, X.; et al. *Nat. Commun.* **2017**, *8*, 14927.
(46) Jin, C.; Kim, J.; Wu, K.; Chen, B.; Barnard, E. S.; Suh, J.; Shi, Z.; Drapcho, S. G.; Wu, J.; Schuck, P. J.; et al. *Adv. Funct. Mater.* **2017**, *27*, 1601741.
(47) Castellanos-Gomez, A.; Buscema, M.; Molenaar, R.; Singh, V.; Janssen, L.; van der Zant, H. S. J.; Steele, G. A. *2D Mater.* **2014**, *1*, 011002.
(48) Berkdemir, A.; Gutiérrez, H. R.; Botello-Méndez, A. R.; Perea-López, N.; Elías, A. L.; Chia, C.-I.; Wang, B.; Crespi, V. H.; López-Urías, F.; Charlier, J.-C.; et al. *Sci. Rep.* **2013**, *3*, 1755.
(49) Gutiérrez, H. R.; Perea-López, N.; Elías, A. L.; Berkdemir, A.; Wang, B.; Lv, R.; López-Urías, F.; Crespi, V. H.; Terrones, H.; Terrones, M. *Nano Lett.* **2013**, *13*, 3447−3454.
(50) Pogna, E. A. A.; Marsili, M.; De Fazio, D.; Dal Conte, S.; Manzoni, C.; Sangalli, D.; Yoon, D.; Lombardo, A.; Ferrari, A. C.; Marini, A.; et al. *ACS Nano* **2016**, *10*, 1182−1188.
(51) Sim, S.; Park, J.; Song, J.-G.; In, C.; Lee, Y.-S.; Kim, H.; Choi, H. *Phys. Rev. B: Condens. Matter Mater. Phys.* **2013**, *88*, 075434.
(52) Vega-Mayoral, V.; Vella, D.; Borzda, T.; Prijatelj, M.; Tempra, I.; Pogna, E. A. A.; Dal Conte, S.; Topolovsek, P.; Vujicic, N.; Cerullo, G.; et al. *Nanoscale* **2016**, *8*, 5428−5434.
(53) Ruppert, C.; Chernikov, A.; Hill, H. M.; Rigosi, A. F.; Heinz, T. F. *Nano Lett.* **2017**, *17*, 644−651.
(54) Sie, E. J.; Steinhoff, A.; Gies, C.; Lui, C. H.; Ma, Q.; Rösner, M.; Schönhoff, G.; Jahnke, F.; Wehling, T. O.; Lee.; et al. *Nano Lett.* **2017**, *17* (7), 4210−4216.

DOI: 10.1021/acs.nanolett.8b02774
Nano Lett. 2018, 18, 6882−6891

(55) Kim, J.; Jin, C.; Chen, B.; Cai, H.; Zhao, T.; Lee, P.; Kahn, S.; Watanabe, K.; Taniguchi, T.; Tongay, S.; et al. *Sci. Adv.* **2017**, *3*, e1700518.
(56) Huber, R.; Tauser, F.; Brodschelm, A.; Bichler, M.; Abstreiter, G.; Leitenstorfer, A. *Nature* **2001**, *414*, 286−289.
(57) Selig, M.; Berghäuser, G.; Richter, M.; Bratschitsch, R.; Knorr, A.; Malic, E. *2D Mater.* **2018**, *5*, 035017.
(58) Ochoa, H.; Guinea, F.; Fal'ko, V. I. *Phys. Rev. B: Condens. Matter Mater. Phys.* **2013**, *88*, 195417.
(59) Ochoa, H.; Finocchiaro, F.; Guinea, F.; Fal'ko, V. I. *Phys. Rev. B: Condens. Matter Mater. Phys.* **2014**, *90*, 235429.
(60) Schmidt, H.; Yudhistira, I.; Chu, L.; Castro Neto, A. H.; Ozyilmaz, B.; Adam, S.; Eda, G. *Phys. Rev. Lett.* **2016**, *116*, 046803.
(61) Molina-Sánchez, A.; Wirtz, L. *Phys. Rev. B: Condens. Matter Mater. Phys.* **2011**, *84*, 155413.
(62) Danovich, M.; Aleiner, I. L.; Drummond, N. D.; Falko, V. I. *IEEE J. Sel. Top. Quantum Electron.* **2017**, *23*, 168−172.
(63) Bertoni, R.; Nicholson, C. W.; Waldecker, L.; Hübener, H.; Monney, C.; De Giovannini, U.; Puppin, M.; Hoesch, M.; Springate, E.; Chapman, R. T.; et al. *Phys. Rev. Lett.* **2016**, *117*, 277201.
(64) Yu, T.; Wu, M. W. *Phys. Rev. B: Condens. Matter Mater. Phys.* **2014**, *89*, 205303.
(65) Yu, H.; Liu, G.-B.; Gong, P.; Xu, X.; Yao, W. *Nat. Commun.* **2014**, *5*, 3876.
(66) Schmidt, R.; Berghäuser, G.; Schneider, R.; Selig, M.; Tonndorf, P.; Malić, E.; Knorr, A.; Michaelis de Vasconcellos, S.; Bratschitsch, R. *Nano Lett.* **2016**, *16*, 2945−2950.
(67) Carvalho, B. R.; Wang, Y.; Mignuzzi, S.; Roy, D.; Terrones, M.; Fantini, C.; Crespi, V. H.; Malard, L. M.; Pimenta, M. A. *Nat. Commun.* **2017**, *8*, 14670.
(68) Marini, A. *J. Phys.: Conf. Ser.* **2013**, *427*, 012003.
(69) Sangalli, D.; Marini, A. *J. Phys.: Conf. Ser.* **2015**, *609*, 012006.
(70) Attaccalite, C.; Grüning, M.; Marini, A. *Phys. Rev. B: Condens. Matter Mater. Phys.* **2011**, *84*, 245110.
(71) Perfetto, E.; Sangalli, D.; Marini, A.; Stefanucci, G. *Phys. Rev. B: Condens. Matter Mater. Phys.* **2015**, *92*, 205304.
(72) Molina-Sánchez, A.; Sangalli, D.; Wirtz, L.; Marini, A. *Nano Lett.* **2017**, *17*, 4549−4555.
(73) Sangalli, D.; Perfetto, E.; Stefanucci, G.; Marini, A. *Eur. Phys. J. B* **2018**, *91*, 171.
(74) Giannozzi, P.; Baroni, S.; Bonini, N.; Calandra, M.; Car, R.; Cavazzoni, C.; Ceresoli, D.; Chiarotti, G. L.; Cococcioni, M.; Dabo, I.; et al. *J. Phys.: Condens. Matter* **2009**, *21*, 395502.
(75) Marini, A.; Hogan, C.; Grüning, M.; Varsano, D. *Comput. Phys. Commun.* **2009**, *180*, 1392−1403.
(76) Kaasbjerg, K.; Thygesen, K. S.; Jacobsen, K. W. *Phys. Rev. B: Condens. Matter Mater. Phys.* **2012**, *85*, 115317.
(77) Palacios-Berraquero, C.; Barbone, M.; Kara, D. M.; Chen, X.; Goykhman, I.; Yoon, D.; Ott, A. K.; Beitner, J.; Watanabe, K.; Taniguchi, T.; et al. *Nat. Commun.* **2016**, *7*, 12978.
(78) Lodahl, P.; Mahmoodian, S.; Stobbe, S.; Rauschenbeutel, A.; Schneeweiss, P.; Volz, J.; Pichler, H.; Zoller, P. *Nature* **2017**, *541*, 473−480.

DOI: 10.1021/acs.nanolett.8b02774
Nano Lett. 2018, 18, 6882−6891